Visiting Scientist mission report

Document NWPSAF-EC_VS-060

Version 1.0

07.06.2022

Development of the SURface Fast Emissivity Model for Ocean (SURFEM-Ocean)

Lise Kilic, Catherine Prigent, Carlos Jimenez

Observatoire de Paris

Development of the SURface Fast Emissivity Model for Ocean (SURFEM-Ocean)

Killic L. Et al., (Observatoire de Paris)

This documentation was developed within the context of the EUMETSAT Satellite Application Facility on Numerical Weather Prediction (NWP SAF), under the Cooperation Agreement dated 7 December 2016, between EUMETSAT and the Met Office, UK, by one or more partners within the NWP SAF. The partners in the NWP SAF are the Met Office, ECMWF, DWD and Météo France.

Change record			
Version	Date	Author / changed by	Remarks
1.0	7.06.22	L Killic	Final

Development of the SURface Fast Emissivity Model for Ocean (SURFEM-Ocean)
-
NWP SAF associate scientist mission NWP_AS20_01

Lise Kilic, Catherine Prigent, Carlos Jimenez

May 31, 2022

1 Introduction

Ocean radiative transfer models in the microwaves simulate the ocean surface emissivity as a function of the frequency, the incidence angle θ, the Sea Surface Temperature (SST), the Sea Surface Salinity (SSS), the Ocean Wind Speed (OWS) and the relative wind direction ϕ. These emissivity models are particularly needed for numerical weather prediction (NWP), for assimilation, as well as for inversion of the geophysical variables.

Previous studies have shown discrepancies between the ocean microwave emissivity models (Kilic et al., 2019; Kilic, 2020). These discrepancies are partly due the different applications of the models (e.g., design for a specific instrument). In the International Space Science Institute (ISSI), a team of experts discussed the latest development in sea surface modelling with recommendations on the next steps for the different aspects of the model (i.e., sea water dielectric properties, wave spectrum, foam coverage and emissivity) (English et al., 2020). The community has converged on a Passive and Active Reference Microwave to Infrared Ocean (PARMIO) model. It is based on the emissivity model developed by Dinnat et al. (2003) at Laboratoire d'Océanographie et du Climat Expérimentations et Approches Numériques (LOCEAN).

The FAST microwave Emissivity Model (FASTEM) (Liu et al., 2011) used in RTTOV does not satisfactorily cover the frequency range from 1.4 GHz to 700 GHz that will be observed by the new generation of european satellite instruments such as CIMR (Copernicus Imaging Microwave Radiometer), MWS (MicroWave Sounder), MWI (MicroWave Imager), and ICI (Ice Cloud Imager). Moreover, FASTEM uses a linear regression scheme that has not been changed since 1990s whereas new Artificial Intelligence (AI) methods are available now.

In this work, we propose a SURface Fast Emissivity Model for Ocean (SURFEM-Ocean) to update FASTEM. PARMIO will be our physical reference model, and the fast version will be developed by using parameterizations based on Neural Networks (NNs). Special efforts will concentrate on extending the frequency range to low (down to 500 MHz) and high frequencies (up to 700 GHz) with a consistent and smooth handling of frequencies, observing incidence angles, and polarizations. Our work will also focus on reducing errors at cold SSTs and high OWSs.

Section 2 describes PARMIO which is the physical ocean emissivity model used as reference to develop SURFEM. Section 3 details the development of SURFEM with the NN training. Section 4 presents the evaluation of SURFEM compared to satellite observations and other ocean emissivity models.

2 Configuration of the physical model

The total ocean surface emissivity with a radiative transfer model is generally written:

$$e_{ocean}(f,\theta,SST,SSS,OWS,\phi) = e_N(f,\theta,SST,SSS) + e_{rough}(f,\theta,SST,SSS,OWS) + e_{azimuth}(f,\theta,SST,SSS,OWS,\phi) \quad (1)$$

where f is the frequency, θ the incidence angle of observation, SST the sea surface temperature, SSS the sea surface salinity, OWS the ocean wind speed, and ϕ the relative wind direction compared to the satellite view direction. e_N is the neutral wind component of the emissivity (i.e. the flat sea emissivity). e_{rough} is the isotropic emissivity due to the roughness of the ocean related to OWS. $e_{azimuth}$ is the anisotropic emissivity due to the roughness of ocean related to OWS and depending on the relative wind direction. It is also current to express the results of an ocean radiative transfer model in terms of brightness temperature (TB_{ocean}) that is directly related to the ocean emissivity e_{ocean} and the SST by the following equation:

$$TB_{ocean} = SST \times e_{ocean} \tag{2}$$

Usually, ocean emissivity models are constituted of: a dielectric constant, a wave spectrum , a foam coverage, and a foam emissivity model. The dielectric constant model simulates the emissivity of the flat sea surface (e_N). It uses a simple or double Debye law (Debye, 1929) whose coefficients are fitted to observations. Then, a wave spectrum, a foam coverage and a foam emissivity models are needed to simulate e_{rough} and $e_{azimuth}$. The wave spectrum model describes the distribution of the waves of the ocean surface. Here there are different type of models: the geometric optic models consider the large-scale waves as an ensemble of facets with different slopes for which the Fresnel reflection applies, and the double-scale model consider the diffusion by the small-scale roughness on each large-scale wave, in addition to the large-scale waves. When the waves break and foam appears, a foam coverage model is used that depends on the OWS and is usually written as a power law (Monahan and O'Muircheartaigh, 1980). Finally a foam emissivity model is needed that depends on frequency and incidence angle.

PARMIO is a double scale ocean emissivity model that can be run with different configurations (i.e. different dielectric constant, wave spectrum, foam coverage and foam emissivity models can be chosen). In its default configuration, which is the LOCEAN model, it is not adapted for high frequencies and we found discrepancies for cold SSTs and high OWSs (Kilic et al., 2019; Kilic, 2020). Here, we will detail the different parameters and modules used, and the development made to improve the accuracy of the PARMIO model.

2.1 Dielectric constants

The dielectric constants from Meissner and Wentz (2004, 2012) used in Remote Sensing Systems (RSS) ocean emissivity model have been chosen for PARMIO. This dielectric constant model has been used widely and tested against satellite observations from 1 to 160 GHz (Kilic et al., 2019; Kilic, 2020). We perform a supplementary test to evaluate if the model extrapolates well for the low frequencies down to 500 MHz and for the high frequencies up to 700 GHz (see Figure 1). The Klein and Swift (1977) model (used in LOCEAN model) is known to be accurate on low frequencies (1 to 10 GHz), whereas Ellison et al. (1998) model (used in FASTEM) is accurate at larger frequencies. For a medium case (SST = 287 K, SSS = 34 psu and $\theta = 50°$), Meissner and Wentz (2012) model shows a difference in emissivity of 0.0003 at 1 GHz with Klein and Swift (1977), and 0.009 at 200 GHz with Ellison et al. (1998).

2.2 Stokes parameters and wind direction

PARMIO is a double scale model as defined in Yueh (1997). The wave spectrum model from Durden and Vesecky (1985) has been chosen with an amplitude coefficient multiplied by 1.25 as it is used in LOCEAN model (Dinnat et al., 2003; Yin et al., 2016) to better fit the low frequency observations. This wave spectrum model has been validated with comparisons against microwave satellite observations in passive mode and with geophysical model functions (GMFs) in active mode.

Observations for the 3rd and 4th Stokes polarizations are limited. We checked the consistency of the wave spectrum model by comparison with different ocean emissivity models as a function of OWS and ϕ. Figure 2 shows the comparisons of the TBs simulated with different ocean emissivity models and PARMIO. The dependencies of the TBs as a function of OWS and ϕ are consistent between the models for all the polarizations. The harmonics are well represented with PARMIO. FASTEM-6 overestimates the amplitude of the harmonics compared to PARMIO and RSS models. Note that comparisons have been done at other key frequencies (not shown here).

To validate further more the selected wave spectrum model and the amplitude coefficient, comparisons are performed in active mode with GMFs. Isoguchi and Shimada (2009), CMOD (Hersbach et al., 2007; Stoffelen et al., 2017), and NSCAT (Wentz and Smith, 1999) GMFs are used for comparisons at L-band, C-band, and Ku-band respectively. Figure 3 shows the backscattering (σ_0) estimated with PARMIO for 3 different amplitude coefficients

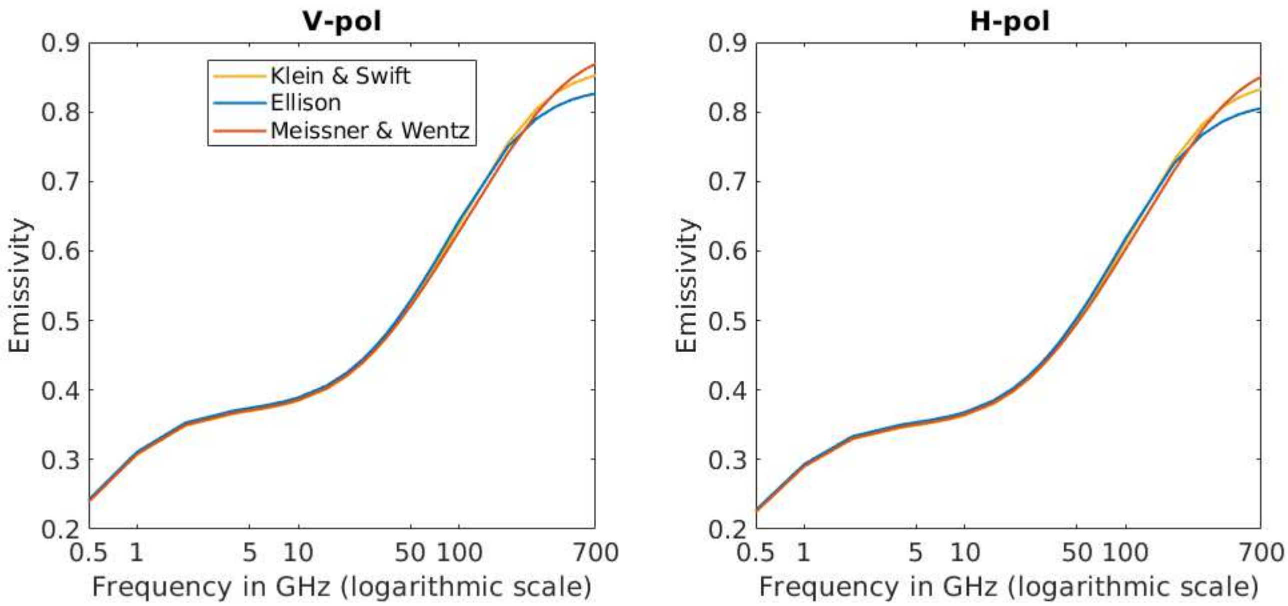

Figure 1: Comparison of 3 dielectric constant models from 500 MHz to 700 GHz for SST = 287 K, SSS = 34psu and $\theta = 50°$.

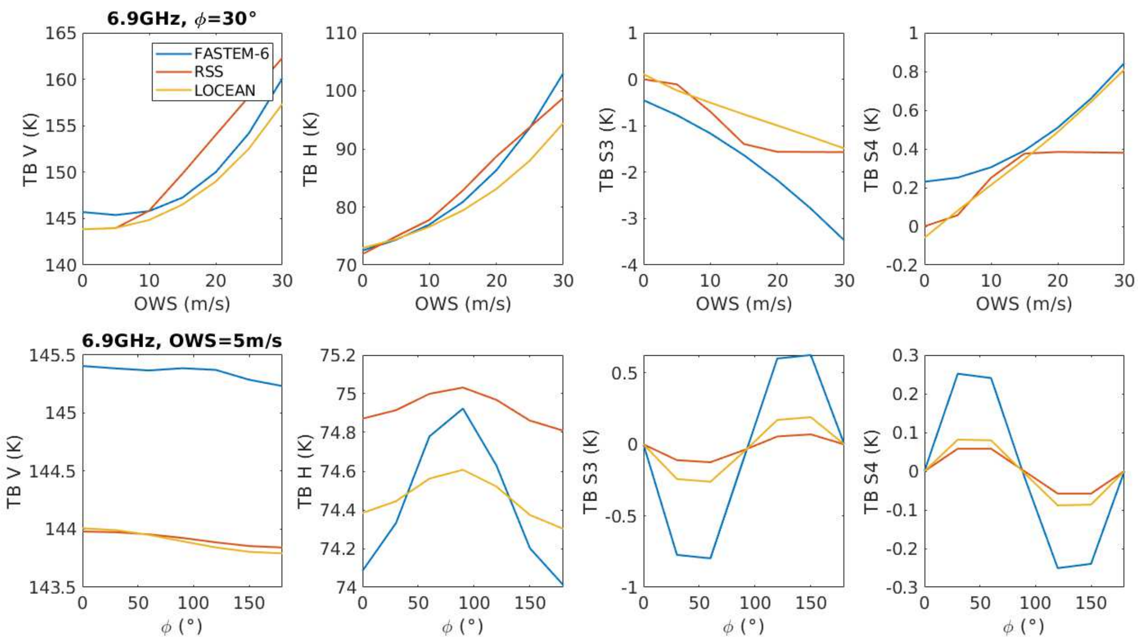

Figure 2: Comparisons of TBs for the 4 polarizations (including 3rd and 4th Stokes parameters) as a function of OWS (1st row) and ϕ (2nd row), at 6.9 GHz and 50° of incidence angle.

of the Durden and Vesecky spectrum, compared to the backscattering estimated with GMFs. Multiplication by 1.25 of the wave spectrum is a good compromise.

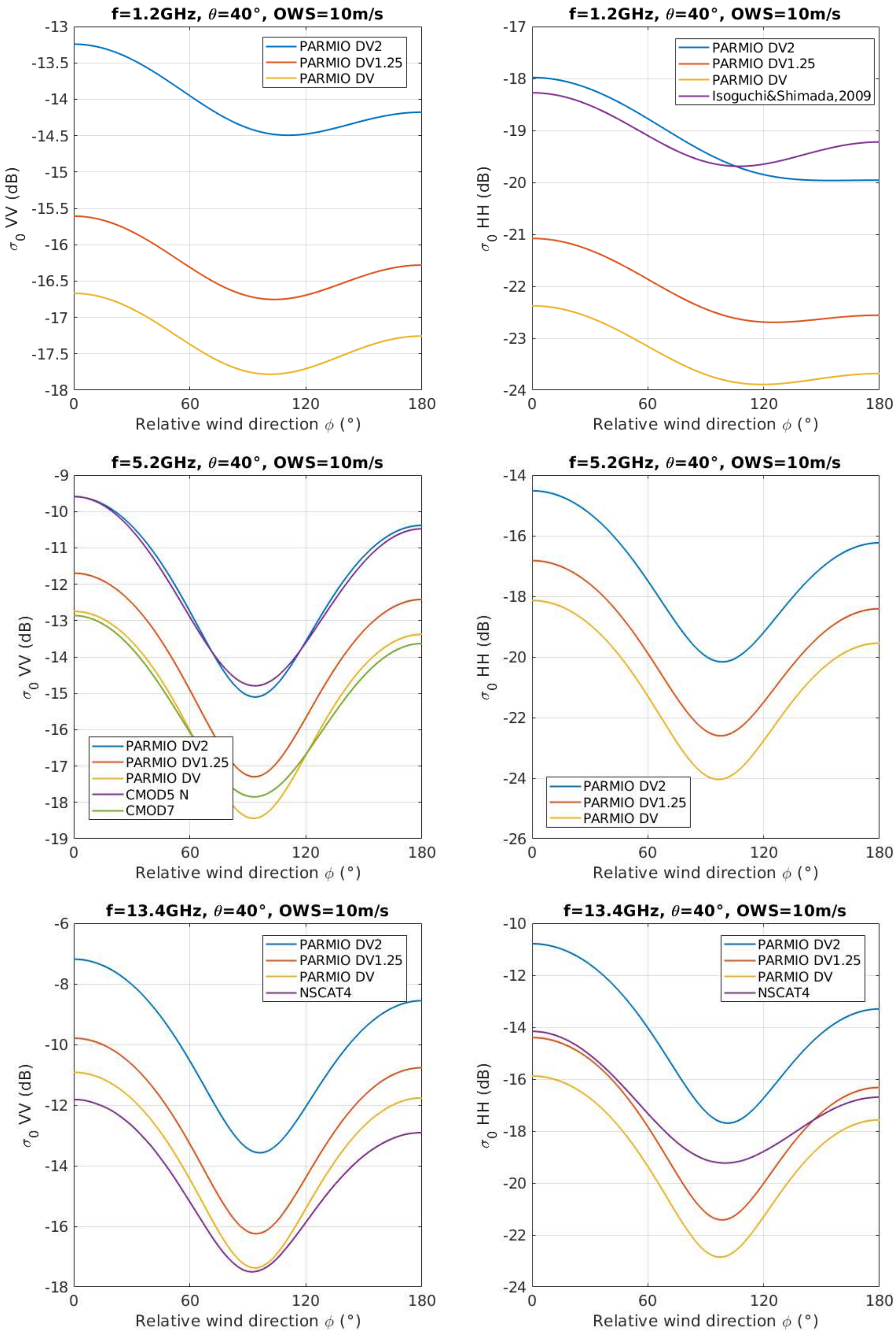

Figure 3: The backscattering (σ_0) in dB as a function of the relative wind direction (ϕ) in degrees, for different Durden and Vesecky (DV) amplitude spectrum coefficient (DV×2; DV×1.25; and original DV). σ_0 VV is on the left column, and σ_0 HH is on the right column. 1^{st} row : L-band ; 2^{nd} row : C-band ; 3^{nd} row : Ku-band.

2.3 Adjustments of the foam parameters

2.3.1 Foam coverage

For the foam coverage, it was decided to use the power law formulation from Monahan and O'Muircheartaigh (1980) with $c = 3$ that correspond to the relation between the foam and the OWS presented in Wu (1979, 1992) by considering neutral stability conditions (i.e. the wind friction velocity is proportional to OWS):

$$Fc = b \times U_{10}^{c} \tag{3}$$

where U_{10} is the OWS at 10 meters beyond the ocean surface.

To determine b, we use all the foam coverage models that adopted the same power law formulation, and we plot b as a function of c. Then we fit the distribution with an exponential law (see Figure 4):

$$b = 0.03516 \times \exp(-2.878 \times c) \tag{4}$$

Therefore, for c=3 we found b=6.25e^{-6}.

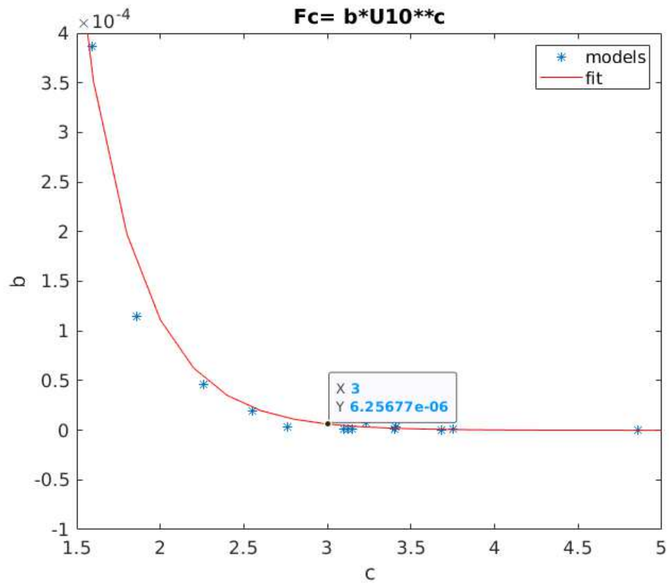

Figure 4: Fit of the b coefficient as a function of the c coefficient for the foam coverages that use the power law formulation of Monahan and O'Muircheartaigh (1980).

The power law of 3 is valid up to 20 m/s then it tends to overestimate the TBs compared to the other models. The models that are directly a parametrization of the observations such as RSS and Hwang et al. (2019) models, show an OWS dependence that is linear after 20 m/s. Therefore, we adapted our foam coverage expression by taking the tangent of our original curve at 20 m/s when the OWS are beyond 20 m/s. Then our foam coverage is expressed:

$$\begin{aligned} &if\ U_{10} < 20 \\ &\quad Fc = 6.25e^{-6} \times U_{10}^{3} \\ &else \\ &\quad Fc = 3 \times 6.25e^{-6} \times 20^{2} \times (U_{10} - 20) + 6.25e^{-6} \times 20^{3} \end{aligned} \tag{5}$$

Results of our foam coverage model using the tangent formulation beyond 20 m/s are shown in Figure 5 and compared with several foam coverages.

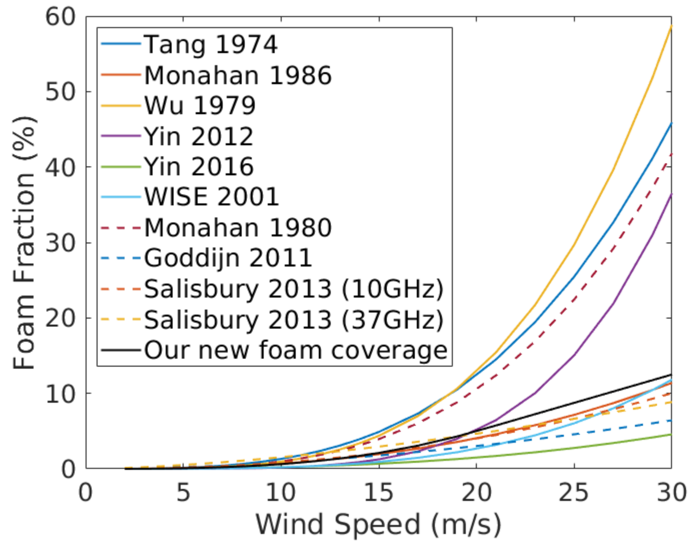

Figure 5: State of the art of the foam coverage models compared to our new foam coverage model in black line.

2.3.2 Foam emissivity

The foam emissivity model from Anguelova and Gaiser (2013) is adopted for PARMIO. This foam emissivity model has different microphysical inputs that can be adjusted to vary the foam emissivity dependence. It is used in the LOCEAN model with the Yin et al. (2016) foam cover and foam emissivity parameters that are adapted for the observations at L-band only. Here, we will adjust these parameters to be accurate on a larger range of frequency given our new foam coverage.

Yin et al. (2016), in their paper vary only two parameters in the foam emissivity of Anguelova and Gaiser (2013): the foam effective thickness (hfe) and the void fraction at the foam-air interface (vaf). The void fraction value at the foam-water interface (vfw) and the shape factor ($m1$) are set to 0.01 and 1 respectively. In this study, only hfe and vaf will vary as in Yin et al. (2016). Using our new foam coverage with Yin et al. (2016) parametrization for the foam emissivity, leads to overestimation of the TBs as a function of OWS at L-band. So the foam emissivity at L-band needs to be reduced to compensate our increase of the foam coverage. To reduce the foam emissivity for lower frequency, hfe has to be decreased. Assuming that the OWS sensitivity tends to saturate at 36 GHz (Kilic et al., 2021), the maximum of foam emissivity has to be reached at 36 GHz.

Given these arguments, different hfe have been tested by analyzing Fig. 5 of Yin et al. (2016) and comparing the results with satellite observations. Finally hfe=2 mm is selected. Different vaf values have also been tested, and vaf=0.97 is selected as the best compromise. It is the same vaf value which is used in Yin et al. (2016) for the model that uses Durden and Vesecky (1985) wave spectrum and the winds of the ECMWF (noted M-Du-E) (which is the parametrization that we use currently for LOCEAN model).

Figure 6 shows the brightness temperature induced by the OWS ($TB_{rough} = e_{rough} \times SST$) as a function of OWS for our reference physical model PARMIO compared to others up to 40 m/s. Hwang et al. (2019) developed a wind induced emissivity model using satellite microwave observations at high OWS. It is used here as a reference for the high OWS (>20 m/s). We can see that SURFEM and Hwang et al. (2019) are close. TB_{rough} of PARMIO is close to LOCEAN at 1.4 GHz, whereas TB_{rough} of PARMIO is increased at 36.5 GHz especially in vertical polarization, as wanted.

3 Development of the fast model

Physical ocean surface emissivity models are slow because of the integration of the radiation coming from different angles and reflected on each wave slope of the rough ocean. AI methods can replicate the emissivity model results faster than using the physical equations. It has been shown that NN techniques are capable of approximating multidimensional geophysical mappings (Krasnopolsky, 2007a), and therefore they are appropriate for a fast modelling

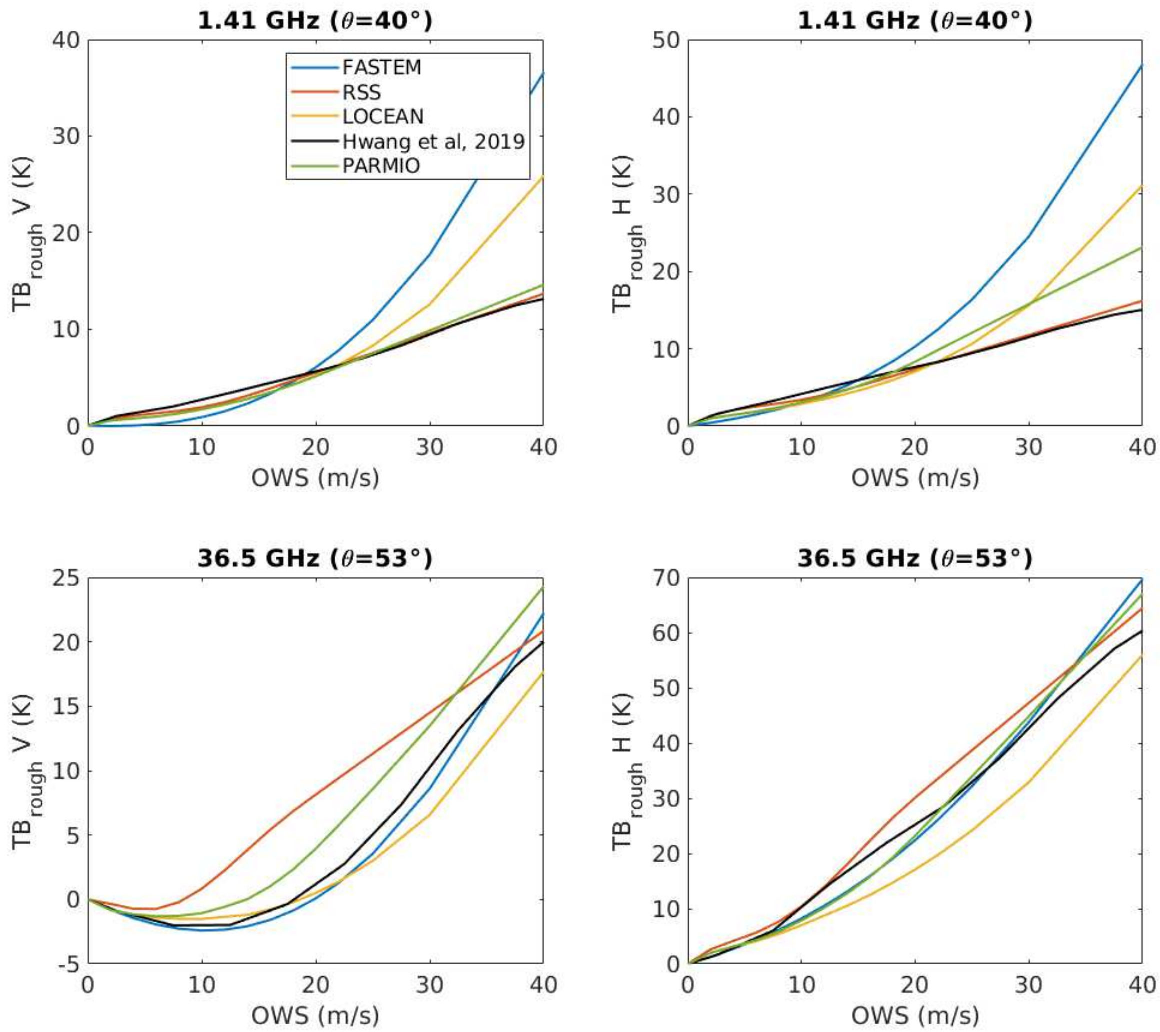

Figure 6: TB_{rough} as a function of OWS for vertical (left) and horizontal (right) polarizations at 1.4 GHz (top) and 36.5 GHz (bottom). SST = 283 K and SSS = 34 psu.

of the ocean surface emissivity once a suitable training dataset is made available (Prigent et al., 2017). Here they will be used to derive the components of the ocean surface emissivities that depend on the OWS, with the training dataset built from the PARMIO emissivity modelling.

3.1 Approach

With PARMIO, the total ocean surface emissivity e is decomposed as follows:

$$e_p = e_pN + e_p0 + e_p1 \times cos(\phi) + e_p2 \times cos(2\phi) \tag{6}$$

where p represents the vertical or horizontal polarizations (v or h), and as follows:

$$e_q = e_q1 \times sin(\phi) + e_q2 \times sin(2\phi) \tag{7}$$

where q represents the 3rd or 4th Stokes polarizations ($S3$ or $S4$). Note that e_p0 corresponds to e_{rough}, and $e_p1 \times cos(\phi) + e_p2 \times cos(2\phi)$ or $e_q1 \times sin(\phi) + e_q2 \times sin(2\phi)$ correspond to $e_{azimuth}$ in Equation 1.

e_pN is the neutral component (no wind) of the ocean surface emissivity. It represents the emissivity of a flat ocean. It can also be expressed in terms of brightness temperature $T_pN = SST \times e_pN$. It is estimated with the dielectric constant module from Meissner and Wentz (2004, 2012) and the Fresnel equations.

$$e_pN = 1 - Rf_p \tag{8}$$

with,

$$Rf_v = \left| \frac{\epsilon cos\theta - \sqrt{\epsilon - sin^2\theta}}{\epsilon cos\theta + \sqrt{\epsilon - sin^2\theta}} \right|^2 \tag{9}$$

$$Rf_h = \left| \frac{cos\theta - \sqrt{\epsilon - sin^2\theta}}{cos\theta + \sqrt{\epsilon - sin^2\theta}} \right|^2 \tag{10}$$

where ϵ is the permittivity of ocean water for a given frequency, SST, and SSS, θ the incidence angle, and Rf_v and Rf_h the Fresnel reflectivities at vertical and horizontal polarization respectively.

The isotropic emissivities (e_v0 and e_h0) and anisotropic emissivities (e_v1, e_h1, $e_{S3}1$, $e_{S4}1$, e_v2, e_h2, $e_{S3}2$, and $e_{S4}2$) are generated by the roughness of the ocean induced by the OWS. These emissivities are slow to compute with physical emissivity models, therefore they will be calculated using NNs. Two NNs will be trained : the first for the isotropic emissivities, and the second for the anisotropic emissivities.

3.2 Neural network settings

A Multilayer Perceptron (MLP) is a type of NN architecture appropriate to approximate multivariate non-linear mappings (Krasnopolsky, 2007a), and it will be applied here to build the fast NN emissivity models. The MLP will contain a first layer with as many input neurons as emissivity predictors, followed by a hidden layer with tansig activation functions, and an output layer with linear activation functions and as many nodes as emissivity components to be predicted. The adaptative parameters of the NN, the weights and biases, are determined during a training phase, using algorithms such as the bayesian regularization backpropagation of Foresee and Hagan (1997). The larger the NN, i.e., the larger the number of weights and biases due to a larger number of hidden neurons, the better the capability of the NN to approximate the mapping. But overfitting, i.e., the NN error is very small for the training dataset, but when new data is presented, the error is much larger, should be avoided. The bayesian regularization backpropagation is the training algorithm preferred here as it is designed to derive NNs that generalize well.

Once the NN is trained, it can be represented by the function:

$$y_q = a_{q0} + \sum_{j=1}^{k} + a_{qj} \cdot tanh(b_{j0} + \sum_{i=1}^{n} b_{ji} \cdot x_i); \quad q = 1, 2...m \tag{11}$$

where x_i and y_q are components of the NN input and output vectors respectively, and a and b are the matrices of the fitting parameters, i.e, the NN weights and biases (Krasnopolsky, 2007b). This analytical function is very fast to be executed, and it is differentiable. Therefore an analytical differentiation of this equation is possible, and this can be used to obtain the first derivatives of the NN outputs over is inputs $\frac{dy_q}{dx_i}$ by simply applying the chain rule for derivatives to the different terms of the equation. These first derivatives can then be used to derive an analytical Jacobian of the function approximated by the NN.

3.3 Neural network training

3.3.1 Training dataset

Our principal dataset to develop and test the NNs is distributed over the classical inputs of ocean emissivity models which are frequency, incidence angle, SST, SSS, and OWS. For frequency, the step is tighter at low frequencies (from 500 MHz to 100 GHz) and become wider when going towards the high frequencies (up to 700 GHz), resulting in more cases to better describe the variability at low frequencies. For incidence angle, the step is regular from 0 to 89° (each 4° with a supplementary point at 89°) to keep the same weight for the NN at each angle. For SST and SSS, the step is large (respectively, each 4°C from -2 to 30°C, and each 10 psu from 0 to 40 psu with a supplementary point at 35 psu), because the output variables of our NNs are weakly dependent on SST and SSS. For OWS, the step is fine and regular (each 2 m/s) from 0 to 30 m/s with 2 supplementary point at 40 and 50 m/s to describe the high OWS with a limited weight on them, as we wish to be more precise for medium OWS (∼5 to 15 m/s). Note that at high OWS (>30 m/s), the physical model has difficulty to converge and to compute the emissivities for some combinations of OWS, frequency and incidence angle.

The principal dataset is then randomly divide in two: 50% are dedicated to the training of the NNs (i.e., training dataset), and the other 50% are dedicated to the testing and validation of the NNs (i.e., validation dataset).

3.3.2 Isotropic emissivities due to the wind

A first NN has been setup to estimate e_v0 and e_h0 the isotropic emissivities due to OWS. The inputs of the NN are the frequency, the incidence angle, the OWS, the SST, the SSS, and the neutral emissivities e_vN and e_hN. Tests have shown that the NN gives better results when e_vN and e_hN are added to the inputs. The outputs of the NN are e_v0 and e_h0.

NNs of different number of neurons in the hidden layer have been tested trained by bayesian regularization backpropagation in order to find the number of weights and biases large enough to properly model the emissivities. A hidden layer with 180 neurons was found adequate after monitoring the NN error on the training dataset and the separated validation dataset.

Figure 7 shows the error of the NN for $T_v0 = e_v0 \times SST$ and $T_h0 = e_h0 \times SST$, by computing the difference between the targets (which are the physical model values) and the outputs (which are the values estimated with the NN) emissivities on the validation dataset. The solid line shows the mean difference, i.e. the bias of the NN that is very close to zero. The dashed line shows the standard deviation of the difference, i.e. the precision of the NN. The NN is less precise where the values of T_v0 or T_h0 are larger e.g., at high OWS (>20 m/s), and at high incidence angle (>70°). Also at low OWS (between 0-5 m/s) for $Tv0$, the NN is less precise because of the large variation of the gradient of $Tv0$ when the incidence angle is large (>70°). The global precision of our NN is 0.22 K for T_v0 and 0.13 K for T_h0.

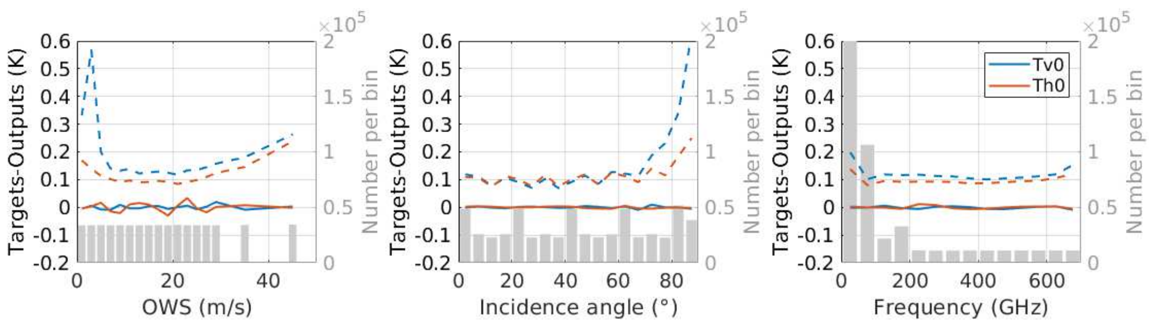

Figure 7: Estimation of the NN error by computing the difference between the targets and the outputs with the validation dataset of T_v0 and T_h0 as a function of OWS, incidence angle (θ), and frequency. The solid line represents the mean error (i.e., the bias) and the dashed line represents the standard deviation (i.e., the precision). The grey bars represent the distribution of the parameters.

Then, the results of our fast model SURFEM are compared with the physical model PARMIO at key frequencies as a function of the OWS in Figure 8. The estimated TBs are very close. At nadir, at OWS = 0 m/s, the horizontal and vertical TBs are equal.

3.3.3 Anisotropic emissivities due to the wind

For the anisotropic emissivities (e_v1, e_h1, $e_{S3}1$, $e_{S4}1$, e_v2, e_h2, $e_{S3}2$, and $e_{S4}2$), the same inputs as previously are used (frequency, θ, OWS, SST, SSS, e_vN, e_hN) and the outputs are the 8 emissivities. As for the isotropic emissivities, 180 neurons in the hidden layer are found adequate to approximate the mapping between the NN inputs and the emissivities.

Figure 9 shows the error of the NN for the 8 anisotropic wind variables by computing the difference between the targets (which are the physical model values) and the outputs (which are the values estimated with the NN).

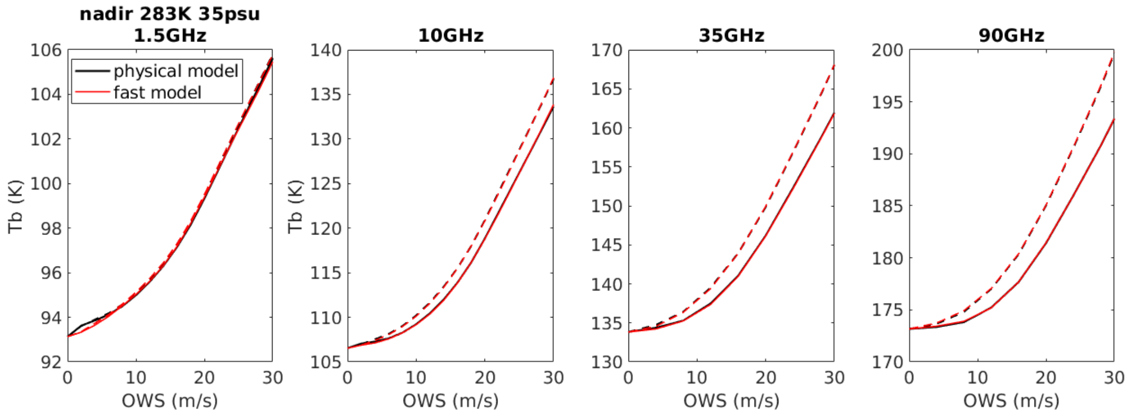

Figure 8: TB as a function of OWS at vertical (solid line) and horizontal (dashed line) polarizations for the physical and the fast models at key frequencies.

The results are given in terms of brightness temperatures ($TB = e \times SST$) for our 8 anisotropic components (T_v1, T_h1, $T_{S3}1$, $T_{S4}1$, T_v2, T_h2, $T_{S3}2$, and $T_{S4}2$). The global mean error (solid line in Figure 9) is close to zero. The global precision of our NN (dashed line in Figure 9) is 0.025 K for T_v1, 0.015 K for T_h1, 0.015 K for $T_{S3}1$, 0.003 K for $T_{S4}1$, 0.035 K for T_v2, 0.027 K for T_h2, 0.038 K for $T_{S3}2$, and 0.017 K for $T_{S4}2$. These errors are very small. Note that the absolute values of these anisotropic wind variables do not exceed 5 K and are generally below 1 K, therefore the relative error of the NN is around 2%.

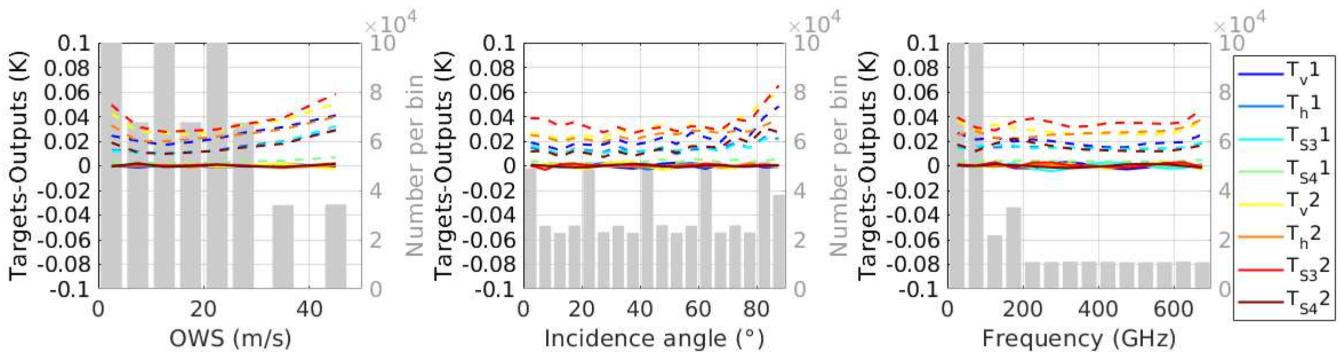

Figure 9: Estimation of the NN error by computing the difference between the targets and the outputs with the validation dataset of T_v1, T_h1, $T_{S3}1$, $T_{S4}1$, T_v2, T_h2, $T_{S3}2$, and $T_{S4}2$ as a function of OWS, incidence angle (θ), and frequency. The solid line represents the mean error (i.e. the bias) and the dashed line represents the standard deviation (i.e. the precision). The grey bars represent the distribution of the parameters.

Then, the results of SURFEM are compared with the physical model PARMIO at key frequencies as a function of the relative wind direction ϕ in Figure 10. The harmonics of the TBs for the four polarizations are well represented with the fast model.

3.4 Computation of the analytical jacobians

Fast computation of the analytical jacobians is required for NWP applications. As SURFEM is partly composed of physical equations (dielectric constant model with double Debye formula and Fresnel equations) and NNs, the jacobians of the total ocean surface emissivity e are computed as follows:

$$\frac{de_p}{dX} = \frac{de_pN}{dX} + \frac{de_p0}{dX} + \frac{de_p1}{dX}cos(\phi) + \frac{de_p2}{dX}cos(2\phi) \tag{12}$$

where X is a geophysical input variable of the model (SST, SSS, or OWS), p the polarization v or h, e_pN the neutral wind emissivity, e_p0 the isotropic wind emissivity, e_p1 the 1^{st} harmonic of the anisotropic emissivity, e_p2 the 2^{nd}

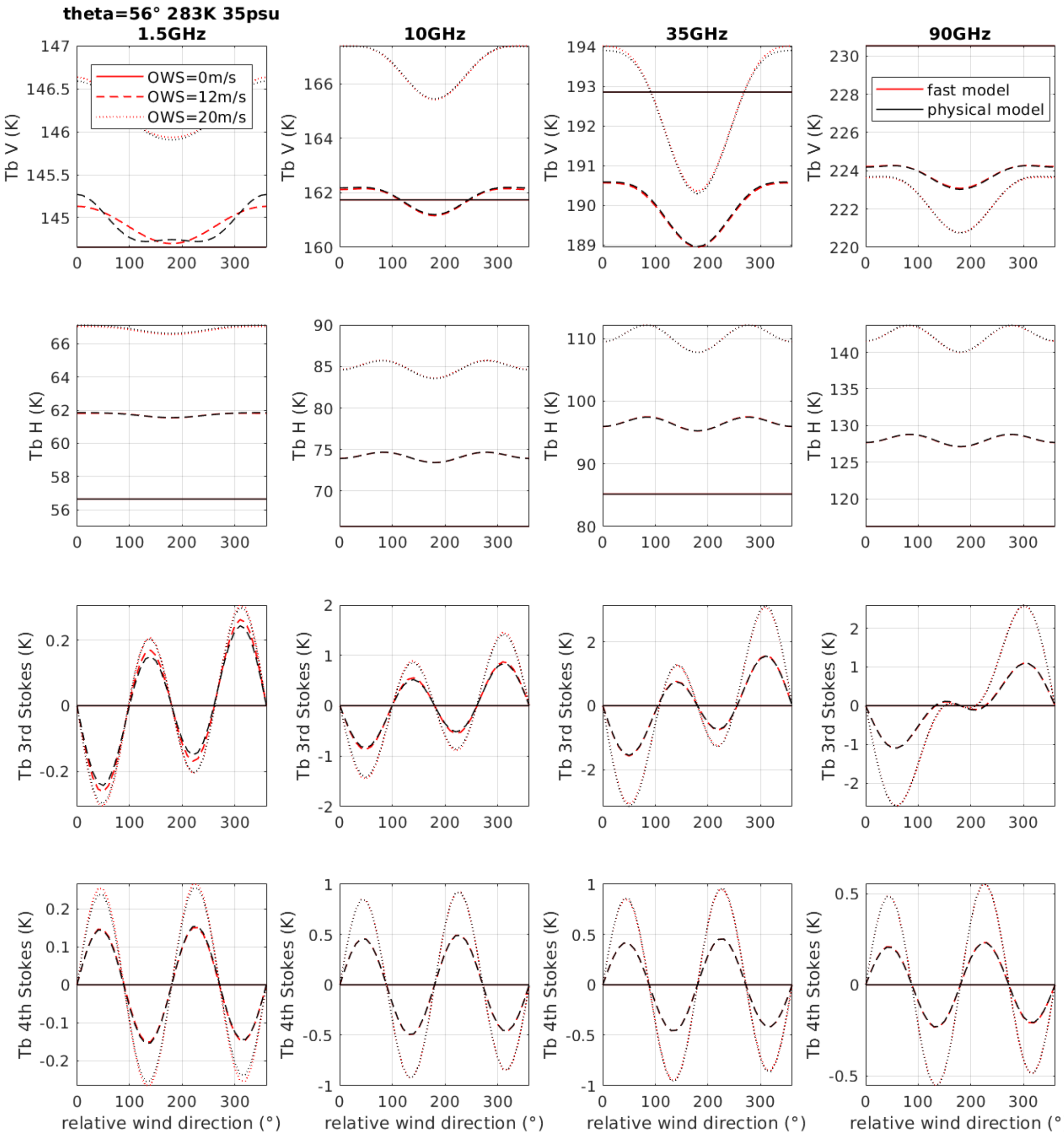

Figure 10: Brightness Temperatures (TBs) as a function of relative wind direction at vertical (1^{st} row), horizontal (2^{nd} row), 3rd Stokes (3^{rd} row), and 4th Stokes (4^{th} row) polarizations for the physical and the fast models at key frequencies for different OWSs.

harmonic of the anisotropic emissivity, and ϕ the relative wind direction. For the 3^{rd} and 4^{th} Stokes polarizations (noted q), the jacobians are written as follows :

$$\frac{de_q}{dX} = \frac{de_q 1}{dX} sin(\phi) + \frac{de_q 2}{dX} sin(2\phi) \tag{13}$$

e_pN only depends on SST and SSS, therefore, $\frac{de_pN}{dOWS} = 0$. To compute $\frac{de_pN}{dSST}$ and $\frac{de_pN}{dSSS}$, the dielectric constant model equations of Meissner and Wentz (2012) and the Fresnel equations have to be derived as follows:

$$\frac{de_pN}{dX} = \frac{d(1 - Rf_p)}{dX} = -\frac{dRf_p}{d\epsilon} \times \frac{d\epsilon}{dX} \tag{14}$$

where X=SST or SSS, Rf_p the Fresnel reflectivity at polarization p and ϵ the dielectric constant. The derivative computations of $\frac{dRf_p}{d\epsilon}$ and $\frac{d\epsilon}{dX}$ are described in Appendix A.

Regarding the computations of the jacobians of e_p1, e_p2, e_q1 and e_q2, they are implemented by the analytical differentiation of the NN functions, as described in Section 3.2 Remind that the inputs of the NNs are: frequency, θ, SST, SSS, OWS, e_vN, and e_hN. The jacobians of the NN are noted $J_N(Y/X)$ where Y is one of the outputs and X one of the inputs of the NN. It is important to note that e_vN and e_hN depend on SST and SSS. Therefore, to compute the derivative of e_p1, e_p2, e_q1 and e_q2 according to SST and SSS, the derivative of e_vN and e_hN have to be taken into account as follows:

$$\frac{de_pi}{dX} = J_N(e_pi/X) + \frac{de_pi}{de_vN} \times \frac{de_vN}{dX} + \frac{de_pi}{de_hN} \times \frac{de_hN}{dX} \tag{15}$$

where i=1 or 2. The same equation is valid for 3rd and 4th stokes polarizations noted q instead of p.

Figure 11 shows the comparisons of the numerical and analytical jacobians of the emissivity computed with SURFEM. Numerical and analytical jacobians match when the step chosen to compute the numerical jacobians is small enough.

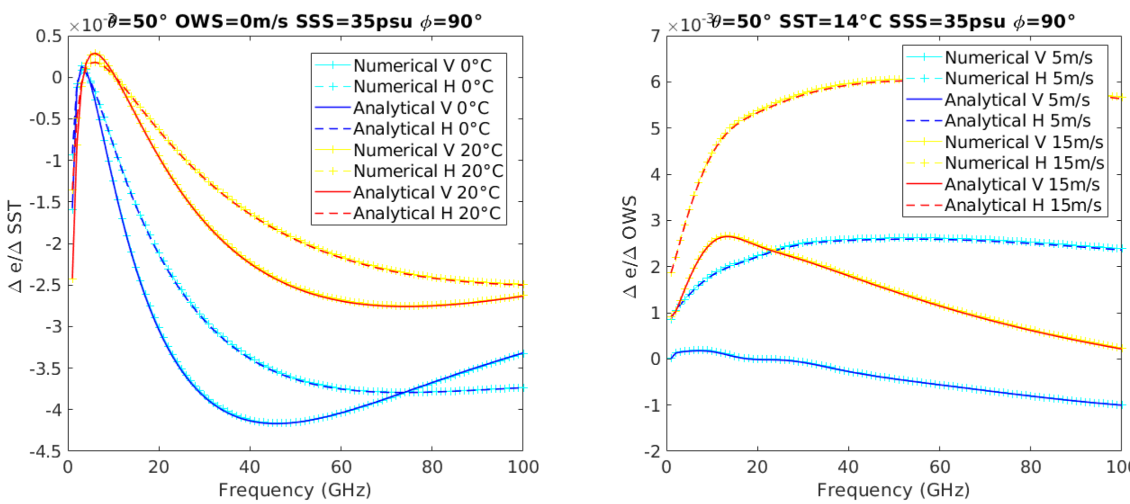

Figure 11: Derivative of the ocean emissivity (Jacobians) along the SST (left) and the OWS (right) as a function of frequency, computed with analytical method versus numerical method.

4 Evaluation of SURFEM

4.1 Satellite observations collocated with ERA5 data

A database of satellite microwave observations over ocean collocated with ECMWF reanalysis (ERA5) data has been created to evaluate the ocean emissivity models. The database contains the observations of SMAP (Soil Moisture Active and Passive), AMSR2 (Advanced Microwave Scanning Radiometer 2), GMI (GPM Microwave Imager), and ATMS (Advanced Technology Microwave Sounder) instruments. They are collocated with the ERA5 data for the surface geophysical parameters, and with the atmospheric transmittance (Tr), the upwelling and downwelling atmosphere brightness temperatures (TB_{up} and TB_{down}) estimated from ERA5 atmospheric data using the Rosenkranz atmospheric radiative transfer model (Rosenkranz, 2017).

We filtered out the sea ice, coastal areas, and the cloudy and rainy pixels. Different methods of filtering have been used depending on the instrument (see Kilic et al. (2019); Kilic (2020)).

4.2 Ocean emissivity models

To evaluate SURFEM, other ocean emissivity models are selected to perform the comparisons. They are the same as in our previous studies (Kilic et al., 2019; Kilic, 2020). Table 1 summarizes the characteristics of the different models that are compared with satellite observations.

Table 1: Summary of the selected Radiative Transfer Models (RTMs) for ocean.

RTM	Model type	Dielectric constant	Wave spectrum	Foam cover	Foam emissivity
LOCEAN Dinnat et al., 2003	Full physical model adjusted for L-band	Klein and Swift, 1977	Durden and Vesecky, 1985 with $a_0 \times 1.25$	Yin et al. 2016	Anguelova and Gaiser, 2013
FASTEM Liu et al., 2011	Parameterized and fast	Ellison et al., 1998 +Double Debye	Durden and Vesecky, 1985 with $a_0 \times 2$	Monahan and O'Muircheartaigh 1986	Kazumori et al., 2008 with Stogryn,1972
RSS Meissner and Wentz, 2012	Empirically fitted to observations	Meissner and Wentz, 2004 and 2012	Wind induced emissivity fitted to observations Meissner and Wentz, 2012 Meissner et al., 2014		
SURFEM Kilic et al.,	Fast using neural networks	Meissner and Wentz, 2004 and 2012	Wind induced emissivity fitted to PARMIO model with neural networks		

4.3 Comparisons

Comparisons of the ocean emissivity models with satellite observations are performed.

To simulate the top of atmosphere brightness temperatures TB_{TOA} observed by the satellite over ocean, the following radiative transfer equation is used:

$$TB_{TOA} = e_{ocean} \times SST \times Tr + R_{ocean} \times TB_{down} \times Tr + Tb_{up} \tag{16}$$

Note that the downwelling signal of the atmosphere is scattered by the rough ocean. This signal is taken into account by FASTEM, LOCEAN and SURFEM model by using a correcting coefficient factor on the reflectivity R_{ocean}. For the RSS model, a TB_{scatt} term is added to the general equation.

Biases (i.e. systematic error) between observations and the models are presented for SMAP and GMI instruments in Figures 12 and 13. They are computed by taking the average of the difference between the observed TBs and the simulated TBs at each channel. For comparison with SMAP, the surface TBs corrected by Remote Sensing Systems are used. SMAP and GMI are well calibrated instruments, therefore the biases observed are reduced. SURFEM shows biases similar to the other models. The biases with SMAP are also calculated with SURFEM at the 3^{rd} and 4^{th} Stokes polarizations and are very small (not shown here).

Figures 14 to 17 shows the difference between the observed and the simulated TBs as a function of OWS, SST, and SSS at 1.4, 10.65, 36.5, and 89 GHz. With SURFEM, the error at high OWS is smaller as well as for cold SST. The error at low frequencies with SURFEM is decreased compared to FASTEM. The error of SURFEM compared to observations is less than 1 K.

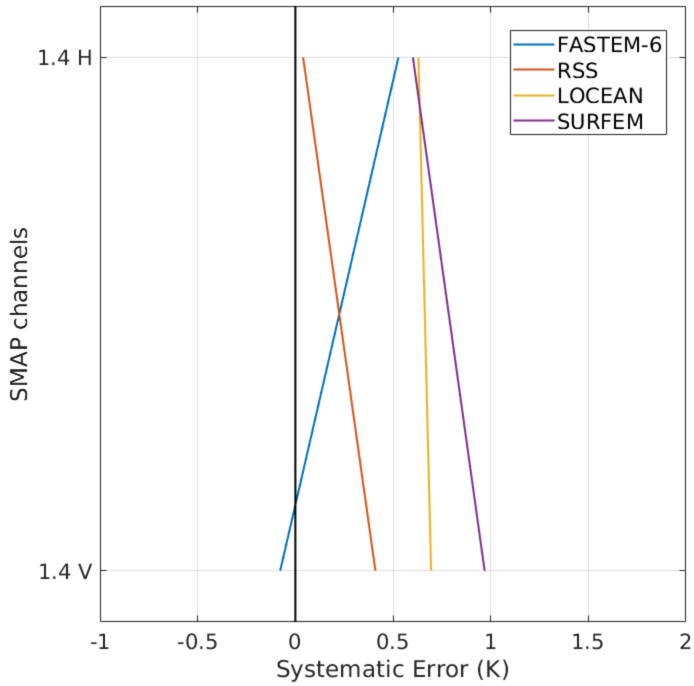

Figure 12: Biases between the ocean emissivity models and SMAP observations ($mean(TB_{obs} - TB_{sim})$).

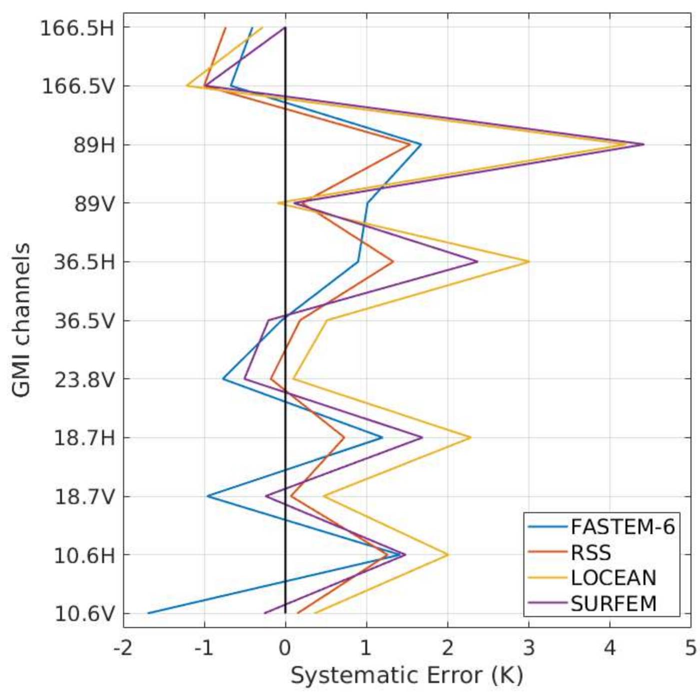

Figure 13: Biases between the ocean emissivity models and GMI observations ($mean(TB_{obs} - TB_{sim})$).

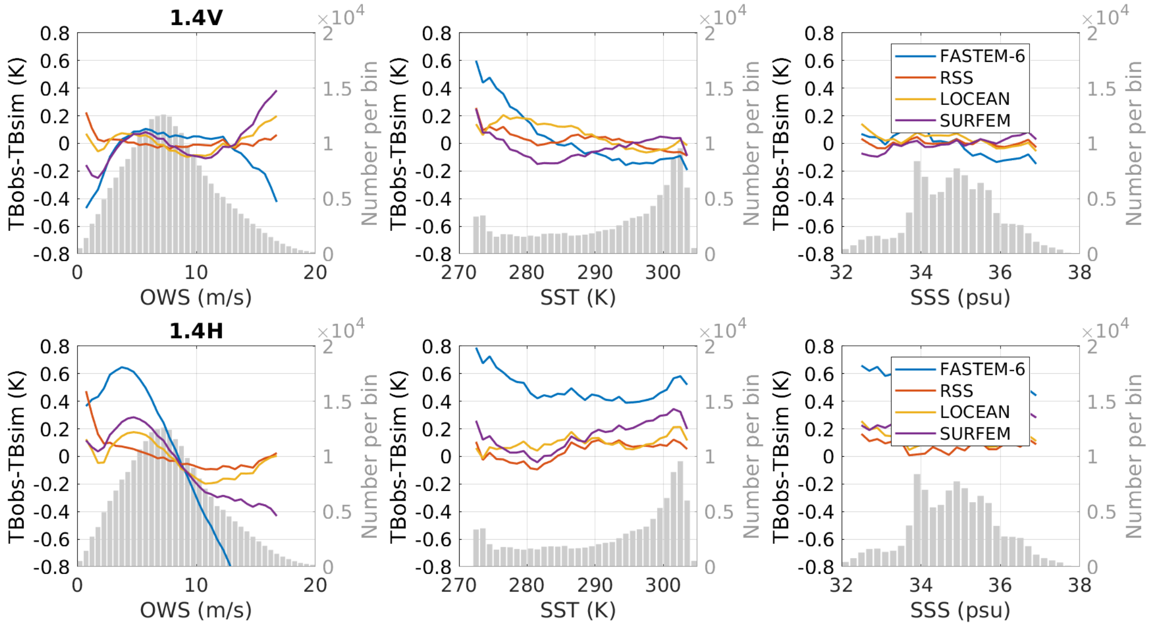

Figure 14: Difference between the SMAP observed TBs and the TBs simulated with the different ocean emissivity models as a function of OWS, SST and SSS at 1.4 GHz.

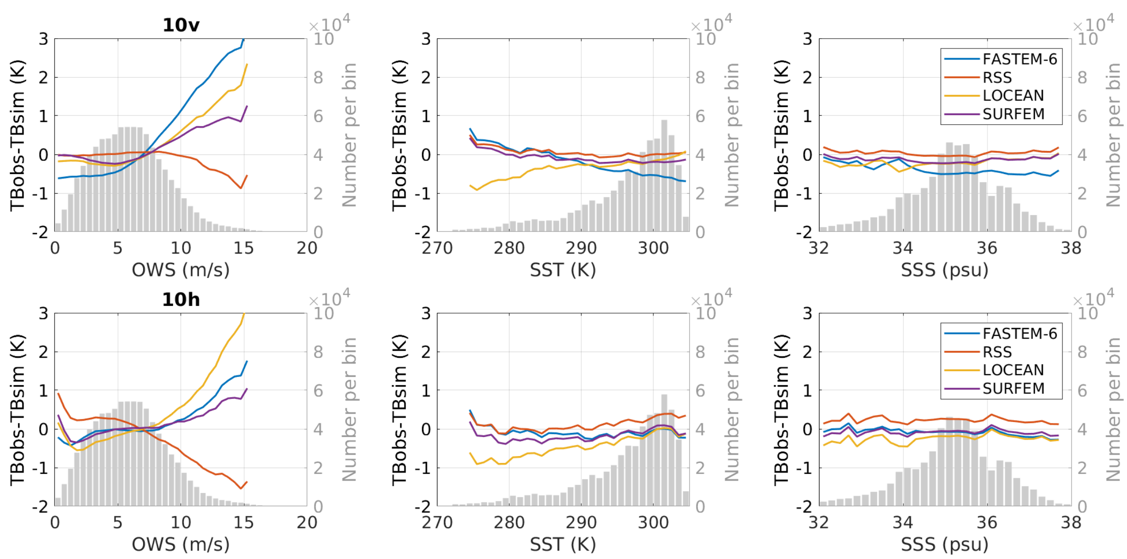

Figure 15: Difference between the GMI observed TBs and the TBs simulated with the different ocean emissivity models as a function of OWS, SST and SSS at 10.65 GHz.

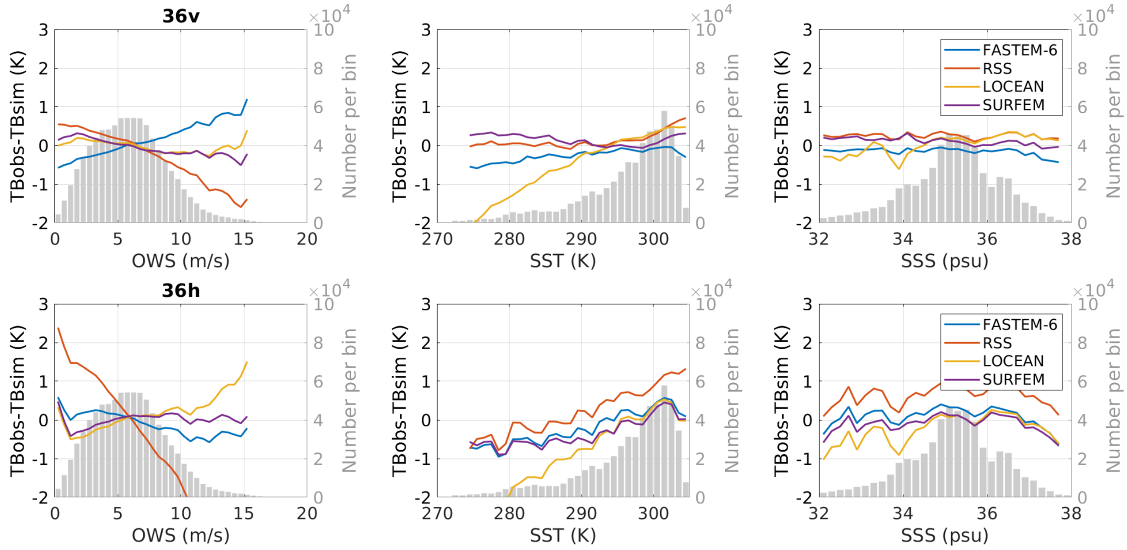

Figure 16: Same as Figure 15 at 36.5 GHz.

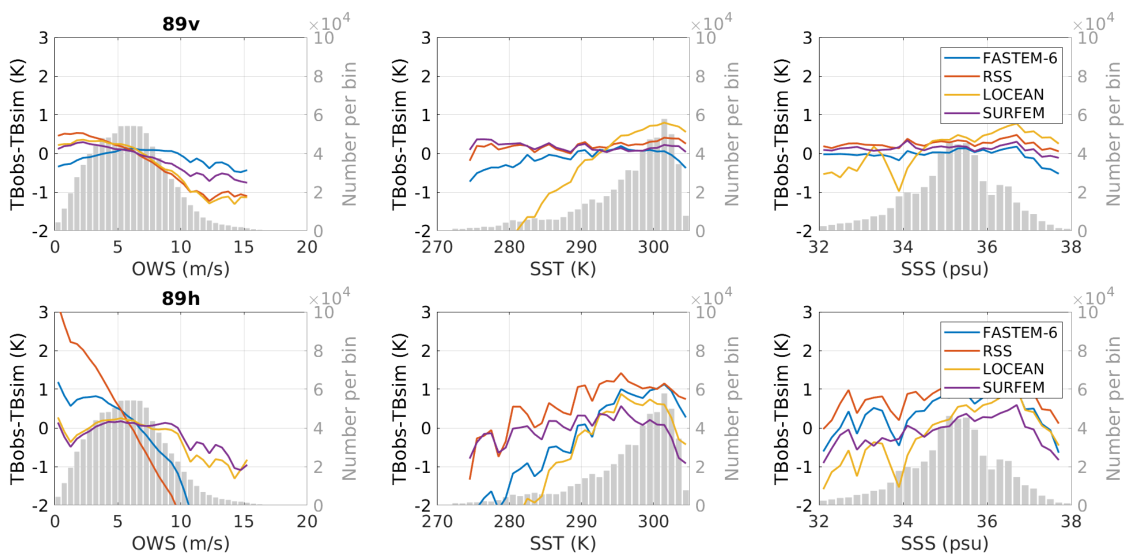

Figure 17: Same as Figure 15 at at 89 GHz.

5 Conclusion

A SURface Fast Emissivity Model for Ocean (SURFEM-Ocean) has been developed. It uses the community physical model PARMIO as reference. The foam coverage and emissivity in the PARMIO model have been updated for an improved agreement with satellite observations over a large frequency range from 500 MHz to 700 GHz. SURFEM covers OWS from 0 to 50 m/s, SST from -2 to 30$°C$ and SSS from 0 to 40 psu. In our approach, SURFEM keeps the physical computation of the neutral emissivity of the ocean (i.e. when there is no wind) by using the dielectric constant of Meissner and Wentz (2012). Then the isotropic and anisotropic emissivities generated by OWS are computed using 2 NNs (one for isotropic signal and the other one for anisotropic signal). The precision of the NNs is better than 0.2 K globally. SURFEM can provide the analytical jacobians of the emissivity along with the surface ocean emissivity for the 4 polarizations (v, h, $S3$, $S4$). Evalutation of SURFEM is performed using the satellites observations collocated with ERA5 data. Comparisons with the observations and the other models show that SURFEM have decreased errors at high OWS and cold SST compared to the initial configuration of PARMIO which is the LOCEAN model. The global error of SURFEM compared to satellite observations is lower than 1 K.

References

Anguelova, M. D. and Gaiser, P. W. (2013). Microwave emissivity of sea foam layers with vertically inhomogeneous dielectric properties. *Remote Sens. Environ.*, 139:81–96.

Debye, P. (1929). *Polar molecules,*. The Chemical Catalog Company Inc., New York.

Dinnat, E. P., Boutin, J., Caudal, G., and Etcheto, J. (2003). Issues concerning the sea emissivity modeling at L band for retrieving surface salinity. *Radio Science*, 38(4).

Durden, S. L. and Vesecky, J. F. (1985). A Physical Radar Cross-Section Model for a Wind-Driven Sea with Swell. *IEEE J. Ocean. Eng.*, 10(4):445–451.

Ellison, W., Balana, A., Delbos, G., Lamkaouchi, K., Eymard, L., Guillou, C., and Prigent, C. (1998). New permittivity measurements of seawater. *Radio science*, 33(3):639–648.

English, S., Prigent, C., Johnson, B., Yueh, S., Dinnat, E., Boutin, J., Newman, S., Anguelova, M., Meissner, T., Kazumori, M., Weng, F., Supply, A., Kilic, L., Bettenhausen, M., Stoffelen, A., and Accadia, C. (2020). Reference-quality emission and backscatter modeling for the ocean. *Bulletin of the American Meteorological Society*, 101(10):E1593 – E1601.

Foresee, F. D. and Hagan, M. T. (1997). Gauss-Newton approximation to Bayesian regularization. In *Proceedings of the 1997 International Joint Conference on Neural Networks*, pages 1930–1935.

Hersbach, H., Stoffelen, A., and de Haan, S. (2007). An improved c-band scatterometer ocean geophysical model function: Cmod5. *Journal of Geophysical Research: Oceans*, 112(C3).

Hwang, P. A., Reul, N., Meissner, T., and Yueh, S. H. (2019). Ocean surface foam and microwave emission: Dependence on frequency and incidence angle. *IEEE Transactions on Geoscience and Remote Sensing*, 57(10):8223–8234.

Isoguchi, O. and Shimada, M. (2009). An l-band ocean geophysical model function derived from palsar. *IEEE Transactions on Geoscience and Remote Sensing*, 47(7):1925–1936.

Kilic, L. (2020). Comparisons of ocean radiative transfer model simulations with gmi observations between 10 and 170 ghz. Technical Report NWPSAF-EC-VS-029, EUMETSAT.

Kilic, L., Prigent, C., Aires, F., Heygster, G., Pellet, V., and Jimenez, C. (2020). Ice concentration retrieval from the analysis of microwaves: A new methodology designed for the copernicus imaging microwave radiometer. *Remote Sensing*, 12(7):1060.

Kilic, L., Prigent, C., Boutin, J., Meissner, T., English, S., and Yueh, S. (2019). Comparisons of ocean radiative transfer models with smap and amsr2 observations. *Journal of Geophysical Research: Oceans*.

Kilic, L., Prigent, C., Jimenez, C., and Donlon, C. (2021). A sensitivity analysis from 1 to 40 ghz for observing the arctic ocean with the copernicus imaging microwave radiometer. *Ocean Science*, 17(2):455–461.

Klein, L. and Swift, C. (1977). An improved model for the dielectric constant of sea water at microwave frequencies. *Oceanic Engineering, IEEE Journal of*, 2(1):104–111.

Krasnopolsky, V. M. (2007a). Neural network emulations for complex multidimensional geophysical mappings: Applications of neural network techniques to atmospheric and oceanic satellite retrievals and numerical modeling. *Reviews of Geophysics*, 45(3).

Krasnopolsky, V. M. (2007b). Reducing uncertainties in neural network jacobians and improving accuracy of neural network emulations with nn ensemble approaches. *Neural Networks*, 20(4):454–461. Computational Intelligence in Earth and Environmental Sciences.

Liu, Q., Weng, F., and English, S. J. (2011). An improved fast microwave water emissivity model. *IEEE Transactions on Geoscience and Remote Sensing*, 49(4):1238–1250.

Meissner, T. and Wentz, F. (2004). The complex dielectric constant of pure and sea water from microwave satellite observations. *IEEE Trans. Geosci. Remote Sens.*, 42(9):1836–1849.

Meissner, T. and Wentz, F. J. (2012). The Emissivity of the Ocean Surface Between 6 and 90 GHz Over a Large Range of Wind Speeds and Earth Incidence Angles. *IEEE Trans. Geosci. Remote Sens.*, 50(8):3004–3026.

Monahan, E. C. and O'Muircheartaigh, I. (1980). Optimal Power-Law Description of Oceanic Whitecap Coverage Dependence on Wind Speed. *J. Phys. Oceanogr.*, 10(12):2094–2099.

Prigent, C., Aires, F., Wang, D., Fox, S., and Harlow, C. (2017). Sea-surface emissivity parametrization from microwaves to millimetre waves. *Quarterly Journal of the Royal Meteorological Society*, 143(702):596–605.

Rosenkranz, P. W. (2017). Line-by-line microwave radiative transfer (non-scattering).

Stoffelen, A., Verspeek, J. A., Vogelzang, J., and Verhoef, A. (2017). The cmod7 geophysical model function for ascat and ers wind retrievals. *IEEE Journal of Selected Topics in Applied Earth Observations and Remote Sensing*, 10(5):2123–2134.

Wentz, F. J. and Smith, D. K. (1999). A model function for the ocean-normalized radar cross section at 14 ghz derived from nscat observations. *Journal of Geophysical Research: Oceans*, 104(C5):11499–11514.

Wu, J. (1979). Oceanic Whitecaps and Sea State. *J. Phys. Oceanogr.*, 9(5):1064–1068.

Wu, J. (1992). Individual characteristics of whitecaps and volumetric description of bubbles. *IEEE Journal of Oceanic Engineering*, 17(1):150–158.

Yin, X., Boutin, J., Dinnat, E., Song, Q., and Martin, A. (2016). Roughness and foam signature on smos-miras brightness temperatures: A semi-theoretical approach. *Remote sensing of environment*, 180:221–233.

Yueh, S. (1997). Modeling of wind direction signals in polarimetric sea surface brightness temperatures. *IEEE Transactions on Geoscience and Remote Sensing*, 35(6):1400–1418.

A Derivative of neutral emissivities

Here we detail the calculations of $\frac{dRf_p}{d\epsilon}$ and $\frac{d\epsilon}{dX}$ with X=T or S for sea surface Temperature or Salinity.

A.1 Derivative of Fresnel equations

We note r_p the unormalized reflectivity terms:

$$r_v = \frac{\epsilon cos\theta - \sqrt{\epsilon - sin^2\theta}}{\epsilon cos\theta + \sqrt{\epsilon - sin^2\theta}} \tag{17}$$

$$r_h = \frac{cos\theta - \sqrt{\epsilon - sin^2\theta}}{cos\theta + \sqrt{\epsilon - sin^2\theta}} \tag{18}$$

r_v, r_h and ϵ are complex numbers. The final Fresnel reflectivities Rf_v and Rf_h are computed as follows:

$$Rf_p = r_p \times \bar{r}_p \tag{19}$$

where the polarization $p = v$ or h, and $\bar{r}_p$ is the conjugate of r_p and expressed as follows:

$$\bar{r}_v = \frac{\bar{\epsilon} cos\theta - \sqrt{\bar{\epsilon} - sin^2\theta}}{\bar{\epsilon} cos\theta + \sqrt{\bar{\epsilon} - sin^2\theta}} \tag{20}$$

$$\bar{r}_h = \frac{cos\theta - \sqrt{\bar{\epsilon} - sin^2\theta}}{cos\theta + \sqrt{\bar{\epsilon} - sin^2\theta}} \tag{21}$$

Our convention is $\epsilon = \epsilon_{re} + i\epsilon_{im}$ then by definition $\bar{\epsilon} = \epsilon_{re} - i\epsilon_{im}$ where ϵ_{re} is the real part and ϵ_{im} is the imaginary part of the complex number ϵ.

Therefore, the derivative of Rf_p as a function of ϵ is written :

$$\frac{dRf_p}{d\epsilon} = (\frac{dr_p}{d\epsilon_{re}} * \bar{r}_p + \frac{d\bar{r}_p}{d\epsilon_{re}} * r_p) - i * ((\frac{dr_p}{d\epsilon_{im}} * \bar{r}_p + \frac{d\bar{r}_p}{d\epsilon_{im}} * r_p)) \tag{22}$$

For vertical polarization ($p = v$):

$$\frac{dr_v}{d\epsilon_{re}} = \frac{cos\theta * (\epsilon - 2sin^2\theta)}{(\sqrt{\epsilon - sin^2\theta} * (\sqrt{\epsilon - sin^2\theta} + \epsilon cos\theta)^2} \tag{23}$$

$$\frac{dr_v}{d\epsilon_{im}} = \frac{icos\theta * (\epsilon - 2sin^2\theta)}{(\sqrt{\epsilon - sin^2\theta} * (\sqrt{\epsilon - sin^2\theta} + \epsilon cos\theta)^2} \tag{24}$$

$$\frac{d\bar{r}_v}{d\epsilon_{re}} = \frac{cos\theta * (\bar{\epsilon} - 2sin^2\theta)}{(\sqrt{\bar{\epsilon} - sin^2\theta} * (\sqrt{\bar{\epsilon} - sin^2\theta} + \bar{\epsilon} cos\theta)^2} \tag{25}$$

$$\frac{d\bar{r}_v}{d\epsilon_{im}} = \frac{-icos\theta * (\bar{\epsilon} - 2sin^2\theta)}{(\sqrt{\bar{\epsilon} - sin^2\theta} * (\sqrt{\bar{\epsilon} - sin^2\theta} + \bar{\epsilon} cos\theta)^2} \tag{26}$$

For horizontal polarization ($p = h$):

$$\frac{dr_h}{d\epsilon_{re}} = \frac{-cos\theta}{\sqrt{\epsilon - sin^2\theta} * (\sqrt{\epsilon - sin^2\theta} + cos\theta)^2} \tag{27}$$

$$\frac{dr_h}{d\epsilon_{im}} = \frac{-icos\theta}{\sqrt{\epsilon - sin^2\theta} * (\sqrt{\epsilon - sin^2\theta} + cos\theta)^2} \tag{28}$$

$$\frac{d\bar{r}_h}{d\epsilon_{re}} = \frac{-cos\theta}{\sqrt{\bar{\epsilon} - sin^2\theta} * (\sqrt{\bar{\epsilon} - sin^2\theta} + cos\theta)^2} \tag{29}$$

$$\frac{d\bar{r}_h}{d\epsilon_{im}} = \frac{icos\theta}{\sqrt{\bar{\epsilon} - sin^2\theta} * (\sqrt{\bar{\epsilon} - sin^2\theta} + cos\theta)^2} \tag{30}$$

A.2 Derivative of the dielectric constant

The permittivity of the ocean water ϵ is expressed as follows with the dielectric constant model of Meissner and Wentz (2012, 2004):

$$\epsilon = \frac{\epsilon_S - \epsilon_1}{1 + i * \nu/\nu_1} + \frac{\epsilon_1 - \epsilon_\infty}{1 + i * \nu/\nu_2} + \epsilon_\infty - i * \frac{\sigma}{2\pi\epsilon_0\nu} \tag{31}$$

The derivative as a function of sea surface temperature (T) is expressed:

$$\begin{aligned} \frac{d\epsilon}{dT} = & \frac{(\frac{d\epsilon_s}{dT} - \frac{d\epsilon_1}{dT}) * (1 + i * \nu/\nu_1) + (\epsilon_S - \epsilon_1) * i * \nu/\nu_1^2 * \frac{d\nu_1}{dT}}{(1 + i * \nu/\nu_1)^2} \\ & + \frac{(\frac{d\epsilon_1}{dT} - \frac{d\epsilon_\infty}{dT}) * (1 + i * \nu/\nu_2) + (\epsilon_1 - \epsilon_\infty) * i * \nu/\nu_2^2 * \frac{d\nu_2}{dT}}{(1 + i * \nu/\nu_2)^2} \\ & + \frac{d\epsilon_\infty}{dT} - \frac{i}{2\pi\epsilon_0\nu} * \frac{d\sigma}{dT} \end{aligned} \tag{32}$$

The derivative as a function of sea surface salinity (S) is expressed:

$$\begin{aligned} \frac{d\epsilon}{dS} = & \frac{(\frac{d\epsilon_s}{dS} - \frac{d\epsilon_1}{dS}) * (1 + i * \nu/\nu_1) + (\epsilon_S - \epsilon_1) * i * \nu/\nu_1^2 * \frac{d\nu_1}{dS}}{(1 + i * \nu/\nu_1)^2} \\ & + \frac{(\frac{d\epsilon_1}{dS} - \frac{d\epsilon_\infty}{dS}) * (1 + i * \nu/\nu_2) + (\epsilon_1 - \epsilon_\infty) * i * \nu/\nu_2^2 * \frac{d\nu_2}{dS}}{(1 + i * \nu/\nu_2)^2} \\ & + \frac{d\epsilon_\infty}{dS} - \frac{i}{2\pi\epsilon_0\nu} * \frac{d\sigma}{dS} \end{aligned} \tag{33}$$

Computations of $\frac{d\epsilon_s}{dX}$, $\frac{d\epsilon_1}{dX}$,$\frac{d\epsilon_\infty}{dX}$, $\frac{d\nu_1}{dX}$, $\frac{d\nu_2}{dX}$, and $\frac{d\sigma}{dX}$ with X = T or S, are long but simple derivatives that are not described here as they will be directly available in the code.